Screw-Tip Soft Magnetically Steerable Needles

Adam J. Sperry, *Student Member, IEEE*, Trevor J. Schwehr, *Student Member, IEEE*, Emma K. Pinegar, Olivia B. Richards, John D. Rolston, *Member, IEEE*, Matthew D. Alexander, Brittany Coats, Jake J. Abbott, *Senior Member, IEEE*, and Alan Kuntz, *Member, IEEE*

***Abstract*—We present a new paradigm in steerable needles comprising flexible tubing with a screw tip and a permanent magnet near the tip. The needle is rotated at its proximal end as the primary mechanism of insertion, rather than being pushed, enabling the screw tip to pull itself through the tissue as it is steered via magnetic torque. Our design enables turns with tighter curvature than previous designs, and it circumvents a well-known problem with existing steerable needles: it is challenging to turn more than 90 degrees without inducing damage. We evaluate our needle via human-in-the-loop robot-assisted magnetic steering in a brain-simulating gel tissue phantom, wherein we achieve a radius of curvature of 29 mm with 210 degrees of turning for a needle with a functional lumen. In a needle without the lumen we achieve a minimum radius of curvature of 10.1 mm. We further evaluate the needle in ex-vivo ovine brain via open-loop steering. We characterize the steerability of the needles as a function of independent parameters. The results demonstrate a needle that promises significantly improved steerability and safety, particularly for use in delicate tissues that create the greatest challenges for existing designs.**

***Index Terms*—Steerable needles, magnetic actuation, continuum robots, steerable cannulas, minimally invasive surgery.**

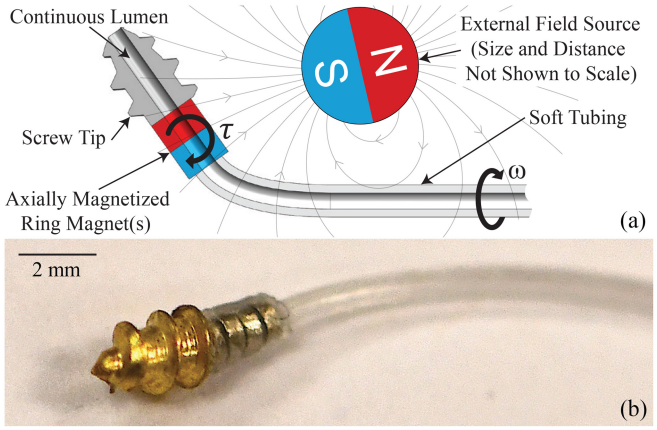

Fig. 1. (a) Schematic depicting cross-section of our needle being steered by the field of an external permanent magnet. Our two control variables are the rotation at the proximal end, ω, and the applied magnetic torque, $\boldsymbol{\tau}$. (b) Example prototype needle made with the tip of a brass wood screw with a machined lumen, four NdFeB ring magnets, and polymer tubing.

I. Introduction

STEERABLE needles that pierce through tissue enable access to locations outside the reach of vasculature or other natural access routes [1], [2], [3]. By steering around sensitive anatomical structures and homing in on targets, they enable targeted delivery of therapy or biopsy at difficult-to-reach locations. Steerable needles show promise for applications in the lung [4], liver [5], kidneys [5], prostate [6], and brain [7].

In this paper, we describe a new paradigm in steerable needles composed of a flexible (*e.g.*, polymer) tube affixed to one or more axially magnetized ring-shaped permanent magnets, which are in turn affixed to a screw tip. The screw may have a central lumen, such that the co-axial lumens of all three elements provide a working channel through the needle (Fig. 1). Whereas the primary mechanism of insertion for most existing designs is to be pushed from their proximal end outside of the body and rotated for steering, our needle is *rotated* at its proximal end as the primary mechanism of *insertion*. This rotation is transmitted through the flexible tube, imparting rotation at the tip, where the screw mechanism enables the needle to pull itself through the tissue from its tip. The needle is steered via an applied magnetic field, which exerts a magnetic torque on the magnet(s) at the needle's screw tip. In our concept, both the device for proximal rotation/insertion and the controlled magnetic field used for steering can be either robotic or manual, which provides flexibility for deployment in future clinical systems.

The vast majority of existing steerable needles designed to pierce through tissue achieve steering by leveraging forces

Manuscript received 31 October 2022; revised 2 January 2023; accepted 16 February 2023. Date of publication 10 April 2023; date of current version 29 January 2024. This article was recommended for publication by Associate Editor B. Lo and Editor P. Dario upon evaluation of the reviewers' comments. This work was supported in part by the National Science Foundation under Grant 1830958. *(Corresponding author: Alan Kuntz.)*

Adam J. Sperry, Emma K. Pinegar, and Jake J. Abbott are with the Robotics Center and the Department of Mechanical Engineering, University of Utah, Salt Lake City, UT 84112 USA (e-mail: adam.sperry@utah.edu; emma.pinegar@utah.edu; jake.abbott@utah.edu).

Trevor J. Schwehr was with the Department of Mechanical Engineering, University of Utah, Salt Lake City, UT 84112 USA. He is now with the Department of Mechanical Engineering, Johns Hopkins University, Baltimore, MD 21218 USA (e-mail: tschweh1@jhu.edu).

Olivia B. Richards and Alan Kuntz are with the Robotics Center and the Kahlert School of Computing, University of Utah, Salt Lake City, UT 84112 USA (e-mail: olivia.richards@utah.edu; alan.kuntz@utah.edu).

John D. Rolston is with the Department of Neurosurgery, Brigham and Women's Hospital, Harvard Medical School, Boston, MA 02115 USA (e-mail: jrolston@bwh.harvard.edu).

Matthew D. Alexander is with the Department of Radiology and Imaging Sciences and the Department of Neurosurgery, University of Utah School of Medicine, Salt Lake City, UT 84132 USA (e-mail: matthew.alexander@hsc.utah.edu).

Brittany Coats is with the Department of Mechanical Engineering, University of Utah, Salt Lake City, UT 84112 USA (e-mail: brittany.coats@utah.edu).

This article has supplementary downloadable material available at https://doi.org/10.1109/TMRB.2023.3265721, provided by the authors.

Digital Object Identifier 10.1109/TMRB.2023.3265721

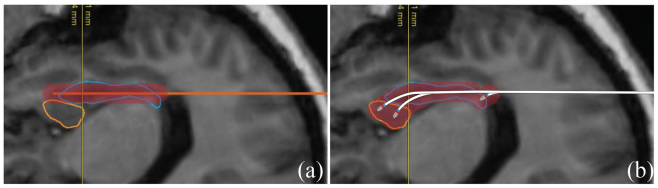

Fig. 2. Motivating example of stereotactic ablation to treat epilepsy. (a) Straight needle insertion and region of ablation with sub-optimal coverage of the hippocampus (blue) and amygdala (orange). (b) Steerable needle insertion and possible region of ablation with three branching paths that more closely follow the shape of the hippocampus and amygdala. The red volume indicates potential ablation coverage in both.

generated through interactions between the insertion force and forces from the tissue itself. The point is for the needles to curve in the tissue; however, pushing a curved needle from its proximal end introduces significant forces on the surrounding tissue at the areas of curvature. These forces can result in damage to tissue via contusion or bleeding due to compression, and can even result in events in which the tissue around the needle fractures and the needle shaft cuts laterally through the tissue, causing significant damage [8]. Further, most steerable needles require tissue stiffness for steering, so that the needle can react against the tissue to cause it to bend. However, this paradigm is particularly problematic when the tissue is delicate, since it is less capable of supporting the loads required for steering and maintaining a curved shape. Finally, as a result of the shaft stiffness required by these types of needles to push them through the tissue from their proximal end, they are incapable of achieving the tight radii of curvature that would be necessary to form expressive paths, regardless of the tissue stiffness. Our needle circumvents the above known problems of existing designs by completely changing the insertion paradigm. As the needle's body only needs to transmit rotation to its tip and not an axial insertion force, our design leverages extremely soft tubing for its shaft, which enables the shaft to have low bending stiffness and impart low forces on surrounding tissues.

Although our new needle promises improved deep-tissue access in a variety of organs, in this work we focus on its potential for use in the brain. In the brain, targeted biopsy and therapy is essential in the diagnosis and treatment of multiple diseases including brain cancer [9], [10], [11], epilepsy [12], [13], and Parkinson's disease [14]. If a needle (which is typically referred to as a cannula in this context) is safely navigated deep in the brain, diagnosis via biopsy [10] and therapies such as gene therapy compounds [14], cell therapy, cellucidal compounds [11], and laser and radiofrequency ablation [9], [12], [13] can be delivered directly to the site at which they can be the most effective. However, there is significant risk associated with current methods, with potential complications including devastating intraparenchymal hemorrhages, leading to paralysis, aphasia, blindness, and other serious neurological problems [10]. To minimize the risk of such complications, a needle or cannula must avoid eloquent areas of the brain, sulci, blood vessels, and ventricles [15].

Consider the case of stereotactic ablation in which the hippocampus and the amygdala are ablated via energy application (*e.g.*, laser or radiofrequency) in order to treat epilepsy [16], [17], [18], [19] (Fig. 2(a)). To minimize damage to healthy brain tissue, this procedure is currently performed by inserting a straight instrument into the structures and ablating in a series of cylindrical shapes. Unfortunately, due to the straight nature of the tool, the desire to avoid ablating brain tissue outside of these structures, and the inability to safely create multiple passes at these brain structures, this results in only partially ablating the intended structures, with 65% and 43% median coverage of the hippocampus and amygdala, respectively [20]. The ability to curve in the brain has the potential to significantly improve this procedure [21]. In this work, we demonstrate the ability to leverage our highly curved needle to more closely conform to these brain structures' complex geometries, conceptually opening the door to better ablation patterns (where the ablation probe could be delivered through, or embedded in, the lumen of the steerable needle). To do so, our needle takes a complex path that incorporates multiple branching points wherein our needle is partially retracted and then steered forward along new paths (Fig. 2(b)). We demonstrate such a complex, multi-branch path in brain-simulating gelatin, covering a planar representation of the relevant brain structures segmented from the real patient scan of Fig. 2, at correct anatomical scale.

This paper extends the work in [22]. We first present the overall design concept of the new needle paradigm followed by a description of needle prototypes and the experimental apparatus used in this work. This is followed by demonstrations of the needle, including example steers, some of which were presented in [22]. We then provide a parsimonious model of steerability, utilizing dimensional analysis, and compare our needle's curvature to that of existing steerable needles. Finally we discuss open problems and the implications of this new paradigm.

II. Related Work

The class of steerable devices designed to pierce through tissue have traditionally been presented under the title "steerable needles" [23]. These designs are composed of a semi-rigid shaft with a sharp tip. The majority of these are inserted from their proximal end, piercing through the tissue at their distal tip, and leveraging a passive asymmetry at their tip to curve through tissue. Webster et al. [24] investigated bevels of different geometry cut into the needle's tip and their influence on steerability. Adding a pre-bent "kink" to the tip of needles was found to increase steerability in tissue phantoms [25] and cadaver brain tissue [7], but comes at the cost of increased tissue damage as the kinked tip cuts a large helical profile in the tissue as it is rotated. To reduce this damaging effect during axial rotation of kinked-tip needles, Swaney et al. [26] incorporated a flexure hinge into the tip of a steerable needle that flexes, effecting a kink-like profile when it is inserted without rotation, but straightening to act as a simple bevel-tip needle without a kink when rotated. This design was later expanded upon with a laser-patterned hinge and helical cutout to reduce shaft stiffness and improve curvature [8].

There also exist designs that leverage active mechanisms to change the needle's tip geometry for steering. A curved stylet inserted through a straight outer cannula has demonstrated

successful steering [27], [28], [29]. A biologically inspired programmable bevel composed of interlocking translational segments steers without axial rotation [30], [31]. A similar design involving a bundle of fibers as a steerable needle was demonstrated in [32]. A needle tip actuated by a pull wire was demonstrated in [33], [34]. Shape-memory alloys have also been used at the tip of a needle for steering [35]. A push-pull mechanism of two segments has also been proposed as a steerable needle [36], [37].

Steerable needles are sometimes conflated with steerable cannulas, including tendon-actuated cannulas [38] and concentric tube robots [39], [40], [41]. To deploy deep in sensitive tissue, these robot's must employ a "follow-the-leader" motion in which the robot's shaft does not change shape after it has been embedded in the tissue. This is possible for these designs, but to do so severely limits the design and prevents them from sufficiently correcting their motion during deployment [28]. Thus, these robots are primarily targeting other applications in which they move through free space.

Of particular relevance to our work are the steerable-needle designs that incorporate magnetics. The concept that is most similar to ours is a concept that uses magnetic torque for steering [42], [43]. As in most steerable-needle designs, this concept relies on a rigid shaft to transmit insertion force to the tip of the needle. However, the authors note damage to the tissue phantom at tight curvatures for their design [42]. It is worth noting that this class of device, as is ours, is related to magnetic catheters (see reviews in [44], [45]), although catheters are designed to navigate natural lumens rather than pierce through tissue.

Another magnetic steerable-needle concept uses magnetic force to pull a needle through tissue using a small permanent magnet affixed to its tip [46]. This design was shown to achieve high curvature values. We note that this concept is related to a "MagnetoSuture" [47], although they do not carry a working channel (which is also the case with many steerable-needle prototypes in the literature). Magnetic force $\boldsymbol{f}$ scales with distance d from the field source as $\|\boldsymbol{f}\| \propto d^{-4}$, which is less favorable at clinical scale than torque $\boldsymbol{\tau}$, which scales as $\|\boldsymbol{\tau}\| \propto d^{-3}$ [45]. This will make clinical translation of benchtop results that rely on magnetic force challenging.

There is a body of literature that has considered the application of untethered magnetic screws, sometimes referred to as microrobots or micromachines, in soft tissue [48], [49], [50], [51], [52]. The basic concept comprises a nonmagnetic screw with a permanent magnet rigidly attached such that its magnetization is *orthogonal* to the screw axis. By applying a rotating magnetic field, the magnetic screw can be both propelled forward and steered, where the axis of rotation of the rotating field indicates the desired forward direction of the screw. A desirable property of magnetic screws is that they can achieve a very tight turning radius—which is a function of the screw, tissue, and magnetic properties [51], as expected—compared to steerable needles; of course, an untethered screw does not carry a working channel. However, if we consider the magnetic torque vector generated at any given instant, we can break it into two components, $\boldsymbol{\tau} = \boldsymbol{\tau}_{\parallel} + \boldsymbol{\tau}_{\perp}$, where $\boldsymbol{\tau}_{\parallel}$ is the component of the torque that is parallel to the screw's axis, which is responsible for propelling the screw forward, and $\boldsymbol{\tau}_{\perp}$ is the component of the torque that is orthogonal to the screw's axis, which is responsible for steering the screw [50]. In practice, we find that $\boldsymbol{\tau}_{\perp}$ is typically only a small fraction of the total available magnetic torque since a relatively large fraction is dedicated to $\boldsymbol{\tau}_{\parallel}$ for the propelling rotation. In addition, the nature of $\boldsymbol{\tau}_{\perp}$ causes a wobble in the path of the magnetic screw (*i.e.*, the screw's path cannot be modeled simply as a circle, but rather, as a spiral wrapped around a circle), and this wobble becomes more pronounced as the magnetic screw is commanded to make tighter turns.

Finally, our device is related to magnetic rotablation catheters [48], [53], [54], [55], which place devices similar to the magnetic screws described above at the distal end of catheters. These devices use the actuation of a rotating magnetic field to replace the mechanical actuation in traditional rotablation catheters. We note that, like magnetic catheters, these devices are designed to move through natural lumens (*i.e.*, blood vessels), which reduces the need for a strong steering torque.

III. Design Concept

Our steerable-needle design represents an innovation over prior designs by combining many of the best aspects of different concepts: it pulls itself through the tissue rather than being pushed, and it leverages magnetic torque, which scales better than magnetic force for clinical translation. This innovation is primarily enabled by the screw tip. In our proposed concept, the magnetization direction of the magnet at the needle's tip is *parallel* to the screw's axis. The result is that all of the available magnetic torque is dedicated to steering, unlike untethered magnetic screws and magnetic rotablation catheters. In addition, none of the wobbling effects of untethered magnetic screws are present in our concept.

A. The Needle

The screw tip of the needle can be fabricated by cutting off the tip of an existing self-tapping screw, or it can be fabricated directly using methods such as additive manufacturing; we demonstrate both of these techniques in this paper. One may hypothesize that it is important to allow the major and minor diameters of the screw tip to become fully developed (*e.g.*, the complete taper as in Fig. 1), which would place a minimum viable length on a given screw tip. An alternate hypothesis is that the tapered tip is not critical, and a threaded rod could be used at the tip. In this paper we demonstrate that needles of both varieties are viable.

The outer diameter (OD) of the ring magnets should not extend beyond the minor diameter of the screw tip to avoid the magnets interfering with the functioning of the screw, and thus the functioning of the needle. An attempt should be made to match the OD of the magnets with the minor diameter of the screw as closely as possible, since the OD enters quadratically into the volume, and thus strength, of the magnets.

If the needle's magnet is comprised of more than one ring magnet stacked together, an adhesive should be used to prohibit the magnets from rotating relative to each other.

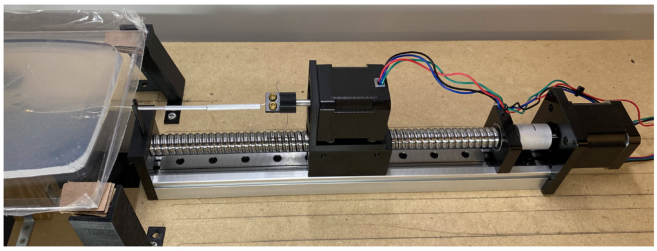

(a) Robotic insertion

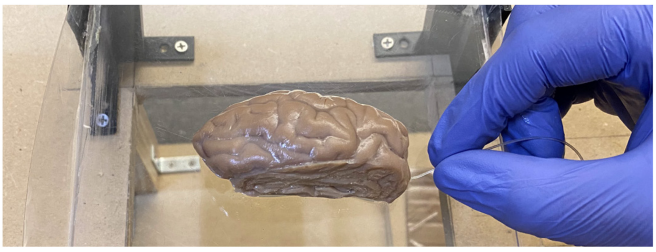

(b) Manual insertion

Fig. 3. We demonstrate rotation/insertion of our needle via two mechanisms. (a) We have designed a robotic device that rotates the needle's tubing at its proximal end, and moves the grasped point forward based on the pitch of the screw tip to ensure there is sufficient slack for the screw tip to pull itself through the tissue, here shown inserting into an agar gel phantom. (b) The needle can be twisted by hand, here shown inserting into *ex vivo* ovine brain.

Otherwise, it will not be possible for the torque applied to the tube to be transmitted to the screw tip for forward motion. In a clinical product, a single custom magnet should be favored over stacked ring magnets; this will lead to a stronger magnet for the same overall package size.

The tube itself can be fabricated from a polymer or a metal, and can even be machined to increase flexibility. Torsional compliance does not negatively impact our ability to steer, as it does with many steerable needles. The tube only needs to have sufficient torsional rigidity to transmit a cutting torque to the screw tip, and ensure the lumen is not compromised.

B. Proximal Rotation and Insertion/Retraction

Rotation at the needle's screw tip is induced by rotating the soft, flexible tube at its proximal end, outside the body. This proximal rotation can be accomplished by a robotic stage, configured for either torque control, angular-position control, or angular-velocity control. The translation of the robotic stage can be passive (*e.g.*, low-friction bearings), active with translation coupled to rotation via the pitch of the screw, active with force controlled to zero, or active with force controlled to some gentle insertion/retraction force. For this study, we developed a simple robotic rotation/insertion system, shown in Fig. 3(a), composed of a linear stage and a rotational stage. The rotational stage turns the flexible tube (and, consequently, the screw tip) while the linear stage advances according to the expected linear motion of the needle based on the pitch of the screw tip. In practice, this was used to maintain a small amount of slack throughout the insertion. A telescoping sheath is used to prevent buckling.

Alternatively, we find that the human hand is adept at manually embodying a desirable proximal rotation/insertion device (see Fig. 3(b)). The benefits of this approach in terms of simplicity are self-evident. In this study, we pursue this method of rotation/insertion as well.

In both methods, the needle is retracted along the path it took in the tissue simply by reversing the direction of rotation. Retraction of the needle does not require any magnetic actuation. Rather, the rotation direction is simply reversed and the tubing removed in a coordinated fashion such that the needle backs itself out of the channel previously made by the needle.

C. Magnetic Steering

In order to steer the needle, we use an applied magnetic field from an external source using the following well-established principles [45]. The small magnet at the needle's tip can be modeled as a magnetic dipole $\boldsymbol{m}_n$ (units A·m^2), which is a vector pointing from its south pole to its north pole with a magnitude that is a product of the volume of the magnet (units m^3) and its material-dependent average magnetization, which is approximately 10^6 A/m for NdFeB. The field $\boldsymbol{b}$ (units T) applied at the location of the center-of-mass of the needle's magnet generates torque $\boldsymbol{\tau}$ (units N·m) that attempts to align the needle's dipole with the applied field:

$$\boldsymbol{\tau} = \boldsymbol{m}_n \times \boldsymbol{b} \tag{1}$$

The field's spatial derivative generates a force $\boldsymbol{f}$ (units N):

$$\boldsymbol{f} = (\boldsymbol{m}_n \cdot \nabla)\boldsymbol{b} \tag{2}$$

We assume herein that the effect of magnetic forces are negligible (*i.e.*, dominated by the effects of magnetic torque), given that magnetic force drops off with distance more quickly than torque, as discussed previously. This assumption becomes increasingly accurate with increased distance from simple field-generation sources. Although we are primarily interested in controlling torque, using field-generation sources with sufficient controllable degrees-of-freedom (see examples in [45]) can enable direct control over the force as well as the torque (*e.g.*, we could control $\boldsymbol{f} \cdot \boldsymbol{m}_n > 0$ to assist insertion).

Although the applied magnetic field can be generated from a variety of permanent-magnet and electromagnet systems, in this study we focus on the use of a single external permanent magnet. The field of the external magnet can be modeled as a point dipole with strength $\boldsymbol{m}_e$. The dipole model is accurate for uniformly magnetized spherical permanent magnets at any distance, accurate for cubic magnets at relatively close distances [56], and increasingly accurate with increasing distance from any field source [45]. The field can then be expressed as

$$\boldsymbol{b} = \frac{\mu_0}{4\pi \|\boldsymbol{p}\|^3}\left(\frac{3\boldsymbol{p}\boldsymbol{p}^\mathsf{T}}{||\boldsymbol{p}||^2} - \mathbb{I}_{3\times 3}\right)\boldsymbol{m}_e \tag{3}$$

where $\mu_0 = 4\pi \times 10^{-7}$ T·m/A is the permeability of free space, $\boldsymbol{p}$ (units m) is the displacement vector from the center of the external magnet to the center of the needle's magnet, and $\mathbb{I}_{3\times 3}$ is the identity matrix. From (1) and (3), it is clear that knowledge of the position and direction of the needle's dipole is necessary to determine the external-magnet pose that will produce a desired torque. Furthermore, there exists a subspace of external-magnet poses that produce the same torque. Some

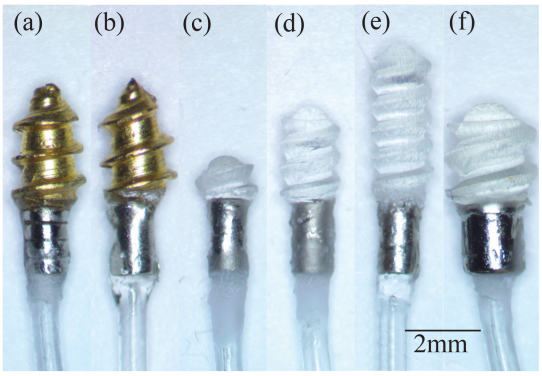

Fig. 4. Images of steerable needle prototypes. (a) Brass-screw-tip needle with ring magnets and a functional lumen. (b) Brass-screw-tip needle with a cylinder magnet. (c)–(f) SLA-printed-screw-tip needles with cylinder magnets used for creating our curvature model. From left to right the value of L is 3.0 mm, 4.3 mm, 5.7 mm, and 4.3 mm. The value of D is 1 mm, 1 mm, 1 mm, and 1.5 mm. L and D are length and diameter, respectively, of the rigid portion of the needle tip as defined in Section VI-A and summarized in Table II.

of these poses may not be feasible, as they would result in a collision with the patient.

Placement of the external magnet can be handled by standard methods for optimization with redundancy and actualized through the use of a robot manipulator with a permanent magnet as its end-effector. It is also conceivable that a clinician could manually position the external magnet to a given target pose, along a trajectory of target poses. This would be unintuitive without assistance, but techniques from image-guided surgery (*e.g.*, [57]) make this a viable approach, provided the (potentially gravity-compensated) weight of the external magnet does not make the task too onerous.

IV. Materials & Methods

Several needle prototypes are used within this study as depicted in Fig. 4. The first needle (Fig. 4(a)) is constructed from the tip of a No. 2 brass wood screw (major dia. 2.2 mm, minor dia. 1.4 mm) with a machined lumen of 0.5 mm diameter. The screw tip is affixed to four axially magnetized Grade-N50 NdFeB ring magnets—each with 0.5 mm inner dia. (ID), 1 mm outer dia. (OD), 0.5 mm thickness—acting as one large magnet with a dipole strength of approximately $\|\boldsymbol{m}_n\| = 0.00133\,\mathrm{A{\cdot}m^2}$. They are affixed using cyanoacrylate to a Tygon tube (formulation ND 100-80) with 0.25 mm ID and 0.76 mm OD. A second brass-screw-tip prototype (Fig. 4(b)) is constructed to be the same as the first where the ring magnets are replaced with a single axially magnetized Grade-N50 NdFeB cylindrical magnet with 1 mm dia. and 2 mm length, thus increasing the dipole strength to $\|\boldsymbol{m}_n\| = 0.0018\,\mathrm{A{\cdot}m^2}$ by sacrificing the working channel (a lumen is still present in the screw tip and the flexible tubing).

For the prototypes of Fig. 4(a)–(b), the screw tip's minor diameter is larger than the magnets' OD by 0.4 mm. By making custom magnets, their OD could be expanded to match that of the minor diameter of the screw tip without interfering with the function of the needle. This would have the effect of increasing the available magnetic torque by 128% for the ring magnet prototype and 96% for the cylinder magnet prototype. Alternatively, in the case of the prototype of Fig. 4(a), both the OD and ID of the magnets could be increased to increase the size of the working channel, potentially with no or limited negative impact on the magnetic torque. The tubing that we use has an ID of only 0.25 mm, which ultimately limits the size of the working channel. Through selection of different tubing, or even the fabrication of custom extruded tubing, the ID of the tubing could be made to match that of the magnets and the screw tip. For the prototype of Fig. 4(a), this would have increased the diameter of the working channel to 0.5 mm.

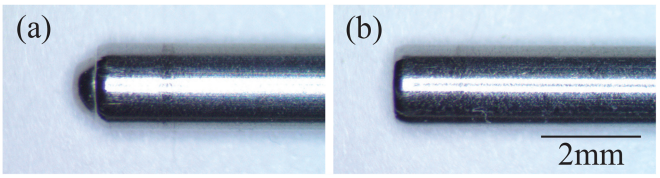

Fig. 5. Image of a clinical-use DBS cannula (a) with coring-prevention insert and (b) with the insert removed. We base our 3D-printed screw geometries on this cannula.

We construct four more needle prototypes for use in modeling steerability. Three of the prototypes (Fig. 4(c)–(e)) are the same as the prototype of Fig. 4(b) except the screw tip is replaced with custom geometries manufactured on a Formlabs stereolithography (SLA) 3D printer. The screw tips are threaded rods (major dia. 1.5 mm, minor dia. 1 mm) with a domed tip that mimic a hypothetical threaded version of a clinically used deep brain stimulation (DBS) cannula with the coring-prevention insert (see Fig. 5). The thread geometry is that of a No. 2 wood screw. These three prototypes differ only in the length of the screw tip with lengths of 1.0 mm, 2.3 mm, and 3.7 mm. Note that for these prototypes, the minor diameter of the screw matches the diameter of the magnet. The fourth prototype used in modeling steerability (Fig. 4(f)) is the same as that of Fig. 4(d) except the screw tip minor diameter and magnet diameter are increased to 1.5 mm resulting in a dipole strength of $\|\boldsymbol{m}_n\| = 0.004\,\mathrm{A{\cdot}m^2}$. To achieve this, the screw geometry of Fig. 4(d) was scaled uniformly (resulting in a major dia. of 2.2 mm) and then shortened to a length of 2.3 mm.

Most of the soft tissue phantoms in this study (Fig. 6(a)) are made of 10–15 mm thick 0.5 wt% agar gel that has been previously established to have similar mechanical properties to human brain [58]. Two additional agar concentrations of 0.325 wt% and 0.625 wt% are used for modeling steerablity in Section VI and comparing our screw-tip needle to prior needle designs in Section VII. All phantoms were left to set overnight in a refrigerator and were allowed to rise to near room temperature (approximately 20–21 °C) before experiments were conducted. Insertion was performed by the robotic stage depicted in Fig. 3(a) and Fig. 6(a).

In this paper, we focus exclusively on the use of a robotically controlled external magnet. In our experimental setup, the pose of the external magnet is controlled by utilizing a spherical-actuator-magnet manipulator (SAMM) [59], mounted as the end-effector of a Yaskawa Motoman six-degree-of-freedom (6-DOF) robotic arm. The

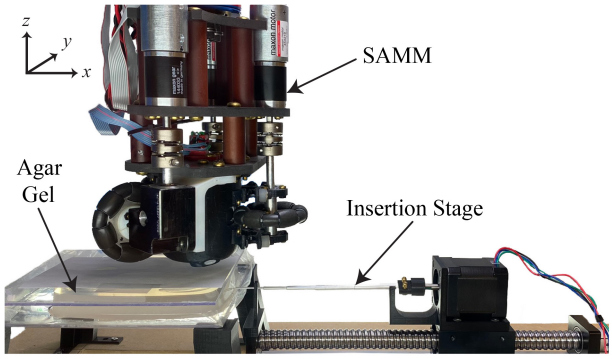

(a)

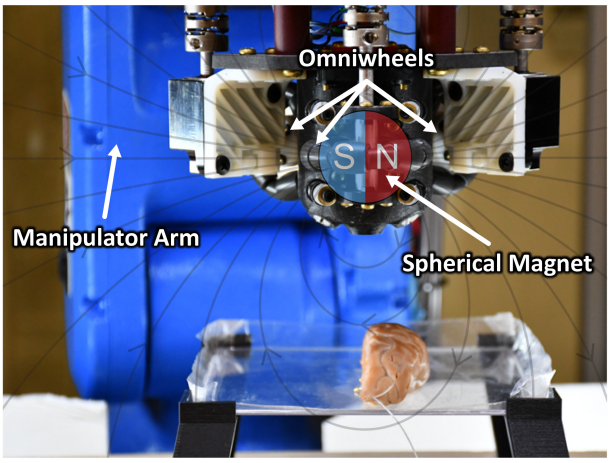

(b)

Fig. 6. (a) Experimental setup with the SAMM positioned above the tip of the needle in the agar gel. The needle is inserted via a robotic insertion stage. (b) Experimental setup with the SAMM positioned above a portion of ovine brain, with the needle inserted in the brain by hand.

SAMM uses three mutually orthogonal omniwheels to act as a singularity-free spherical wrist capable of controlling a 50.8 mm diameter spherical Grade-N42 NdFeB permanent magnet with dipole strength $\|\boldsymbol{m}_e\| = 66.0\,\mathrm{A{\cdot}m^2}$ to arbitrary orientations (Fig. 6). This combination of SAMM and robot arm makes arbitrary external magnet poses possible. Such a system could be scaled to clinical scale to realize the concept depicted in Fig. 2. However, note that the continuous-rotation capability of the SAMM is not necessary for this application, and a simpler robot-controlled magnet could be used.

Although the application of torque from arbitrary positions is a solvable problem, and the governing actuation equations are presented in a vector form that is suitable for planning and control in 3D, in our experiments that follow we chose a special configuration in which the external magnet is always directly above the needle's magnet (*i.e.*, $\boldsymbol{p}$ is in the $-\boldsymbol{z}$ direction) and $\boldsymbol{m}_e$ is perpendicular to $\boldsymbol{p}$ (see Fig. 6(a)). If $\boldsymbol{m}_n$ is in the horizontal plane, then $\boldsymbol{\tau}$ is always parallel to $\boldsymbol{p}$, producing trajectories in the horizontal plane. Under these conditions, the scalar equation for the torque about the vertical axis (*i.e.*, in the steering plane) is

$$\tau = \frac{\mu_0 \|\boldsymbol{m}_n\| \|\boldsymbol{m}_e\|}{4\pi \|\boldsymbol{p}\|^3} \sin\theta \tag{4}$$

where $\theta \in [-180°, 180°]$ is the angle from $\boldsymbol{m}_n$ to the applied field $\boldsymbol{b}$, measured about the $\boldsymbol{z}$ axis.

We chose to apply the maximum torque for a given $\|\boldsymbol{p}\|$, which occurs when $|\theta| = 90°$. In this way, the magnitude of the torque can be controlled by controlling $\|\boldsymbol{p}\|$. In this orthogonal configuration, the magnetic force is exactly zero (assuming perfect alignment). In this paper we used a range of $\|\boldsymbol{p}\|$ from 43 mm to 66 mm (scaling discussed in Section VIII).

Given the above configuration for the application of magnetic torque, the necessary localization of the screw tip reduces to finding its 3-dimensional planar pose (*i.e.*, position in the xy-plane and heading orientation θ_n). In our study this localization is performed by a human using a pair of orthogonal calibrated cameras and a SpaceExplorer 3D mouse. One camera is positioned below the agar gel (*i.e.*, pointed in the $+z$ direction) and provides the primary view of the needle tip's planar pose. The other camera is positioned on the side of the agar gel (*i.e.*, pointed in the $+y$ direction) and is used to get the z height of the needle which enables perspective calibration in the primary view. A virtual pose is projected onto each view and the human uses the 3D mouse to align the virtual pose with the actual needle tip pose. This localization is performed every 1 mm of insertion. We note that the needle height is inferred from the insertion point rather than from the actual needle tip because the gel is opaque beyond 5–10 mm of depth from the side view (*i.e.*, we are not actively localizing or controlling the z position of the needle tip). The human also has control over the direction and magnitude of the torque as well as initiating an insertion step and the speed of insertion. In this way, for our subsequent experiments, the human is acting as the localizer, trajectory planner, and controller when required to perform closed-loop control of the needle.

Resulting curvature is measured by fitting a circle using a least-squares approach to the recorded 2D positions of the needle tip during insertion. To calculate the local curvature at each point along the trajectory, we used direct least-squares fitting as outlined in [60], using a 40-point moving window.

V. Demonstrations of Steerability

In this section, we provide a variety of demonstrations of the steering capability of our needle. Our first demonstration shows clinically relevant steering in brain, which demonstrates the ability of our needle concept to realize the therapy depicted in Fig. 2. These experiments were performed using the needle with a functional lumen shown in Fig. 4(a). A correct to-scale image of the human brain, with the hippocampus and the amygdala regions highlighted, was placed above the agar gel such that it could be seen through the agar by the camera below and used as reference for the human-driven steering. A human operator then attempted to steer a three-branched, curved trajectory that ensured that the aggregate path covered the geometry of both brain structures assuming cylindrical ablation around the needle tip trajectory (see Fig. 2(b) for the desired trajectory). Figure 7 shows an example three-stage branching path achieved by our needle. Sub-path 1 is the first insertion of the needle. Sub-paths 2 and 3 were achieved by partially retracting the needle to the respective branching point

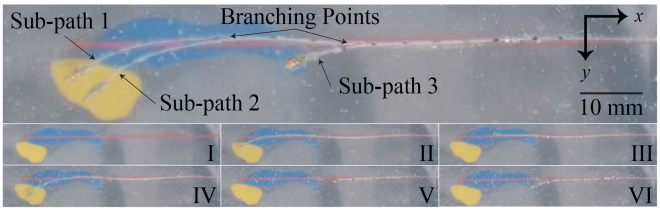

Fig. 7. (Top) Composite image of the branching paths achieved with our needle, with at-scale image of brain structures. (Bottom) Chronological image sequence.

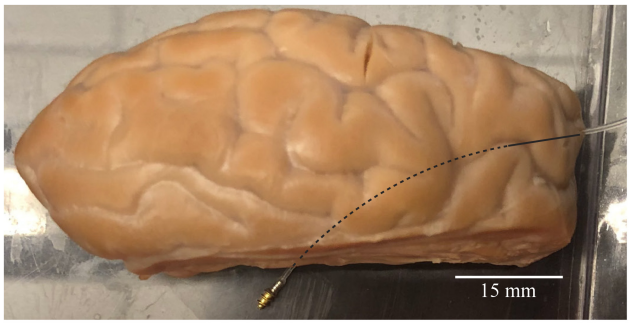

Fig. 8. Example of steering through ovine brain (top-down view). The needle enters at the right of the image and exits at the bottom of the image. In this case, the needle was rotated at its base by hand rather than with the robotic insertion stage. We steered the needle open-loop by estimating the needle tip's pose based on expected curvature and translation. Due to the open-loop nature of this experiment, this curvature should not be assumed maximal. The solid line approximates the 10 mm straight portion of the path of the needle, and the dashed line approximates the curved portion of the path, which has an RoC of 52 mm. Note that an adult human brain is significantly larger than the ovine brain shown here, with more than 2× both length and width [61].

then reinserting while steering in the new direction of each sub-path. We achieved a 26 mm minimum radius of curvature (RoC) using an applied field strength of 73 mT. Video of the steer can be found in the multimedia attachment accompanying this work.

In order to verify our device is capable of steering in biological tissue, we conducted a steering trial in the right hemisphere of an *ex vivo* ovine brain. This experiment was again performed using the needle of Fig. 4(a). The steering was performed open-loop due to the opacity of brain tissue. Before inserting the screw tip, a small incision was made with a scalpel to allow the screw to bypass the tough membrane on the outside of the brain. After inserting the screw tip into the incision, we twisted the needle by hand, providing minimal forward pressure while still allowing the tube to advance approximately 10 mm into the tissue. We used our computer-vision set-up to measure the insertion point in the workspace, assumed 10 mm of straight travel, and then calculated a set of waypoints (position and heading) every 1 mm along the circumference of an arc in the horizontal plane. We assumed an average RoC of 41 mm from pilot steers for use in our open-loop model. We then lowered the SAMM to directly above the surface of the brain at the starting location of the arc, with the correct orientation. This resulted in using an applied field strength of 39.7 mT. We then manually inserted the needle in 1 mm increments, stopping to update the SAMM to keep up with the assumed needle pose. This process was repeated until the screw exited the tissue. A photo of the needle having passed through the brain is shown in Fig. 8. This experiment demonstrates the effectiveness of our proposed needle in moving through real brain tissue. From post-processing, we found that we achieved an RoC of approximately 52 mm. Note that due to the open-loop steering strategy this RoC should not be considered necessarily representative of what would be achievable in brain tissue with closed-loop control and instead this experiment is intended to demonstrate the needle's ability to qualitatively steer in brain tissue.

Next, we demonstrate complex and high-curvatures steers using the needle of Fig. 4(b) in the agar-gel phantom. We first inserted the needle straight to a depth of 15 mm with no magnetic steering. Then we steered with a constant applied field of 72.4 mT. This needle achieved an RoC of 12.8 mm, total insertion depth of 65 mm, and total turn of 210°. The resulting steer is shown in Fig. 9(a). In this instance, the needle has reached a maximum depth as the tubing has begun to twist on itself. We believe that this maximum depth is trajectory dependent. An S-curve steer using this same needle under the

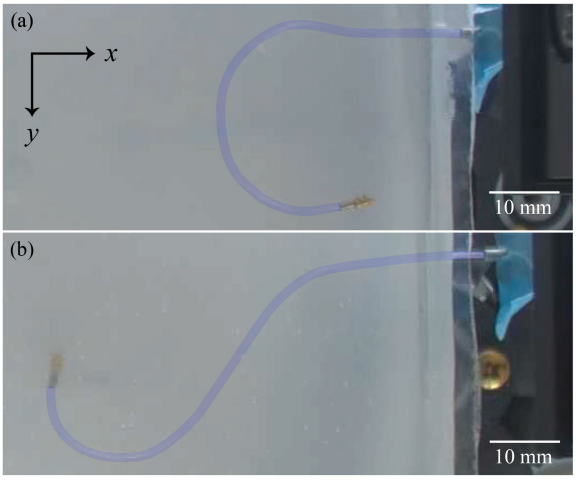

Fig. 9. (a) Steer achieving 12.8 mm RoC, 65 mm insertion depth, and turning through 210°. (b) S-curve steer achieving minimum RoC of 10.1 mm and an insertion depth of 76 mm. The flexible tube is highlighted in blue for visibility purposes.

same conditions is depicted in Fig. 9(b). This steer consists of steering in one direction for a quarter circle and then steering in the opposite direction for a half circle, with a total insertion depth of 76 mm and a minimum RoC of 10.1 mm on the last portion of the steer. In this steer, the needle has not reached a maximum depth. We believe the tighter RoC in this steer compared to the steer of Fig. 9(a) is due to the needle tip rising in the gel phantom, thus decreasing $\|\boldsymbol{p}\|$ and increasing the applied torque. Video of these steers can be found in the multimedia attachment accompanying this work.

Given that most of the experiments in this work are limited to planar trajectories, we provide an example of out-of-plane steering to demonstrate that our needle concept can in fact produce 3D trajectories. Figure 10 shows two steers using the needle of Fig. 4(a) in which the needle is steered down away from the SAMM (Fig. 10(a)) and up toward the SAMM (Fig. 10(b)). We emphasize the fact that we are able to steer away from the strong external magnet, which may tend to

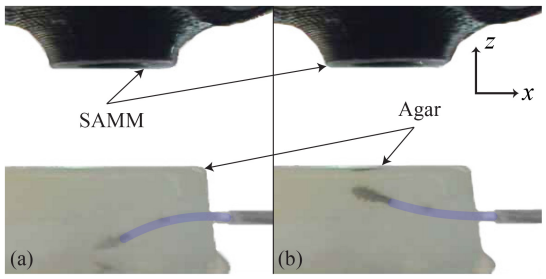

Fig. 10. Demonstration of out-of-plane steering (side view). We steered down (a), partially retracted, then steered up (b). The flexible tube is highlighted in blue for visibility purposes.

exert an attractive force on the needle tip, due to the dominant effect of magnetic torque in the steering.

VI. Modeling Steerability

In this section, we characterize the steerability of our soft needles. To characterize steerability, we naturally turn to a characterization of the instantaneous curvature κ that we can generate at the distal end of our needle (*i.e.*, at the distal end of the compliant tube, since the magnetic-screw tip is rigid). We begin by using dimensional analysis to find a minimal representation of the independent nondimensional parameters that affect curvature. We then perform experiments to characterize curvature in this nondimensional parameter space. Finally, we use linear regression to find a parsimonious model that describes our experimental data.

A. Dimensional Analysis

We expect a basic model of curvature to be a function of up to seven variables in general:

1) the cross-sectional geometry of the compliant tube, which is encoded in its area moment of inertia, I;
2) the material of the compliant tube, which is encoded in its modulus of elasticity, E;
3) the length of the rigid magnetic-screw tip, L, which does not include the tapered portion at the front of the tip (which is assumed to be present regardless of L);
4) the outer diameter of the permanent magnet, D, which should be equal to the minor diameter of the screw to maximize potential magnet volume;
5) the applied magnetic torque, τ;
6) the modulus of elasticity of the soft tissue, E_{st}; and
7) Poisson's ratio of the soft tissue, ν_{st}.

It would be reasonable to assume that the length of the proximal portion of the compliant tube that is already embedded in the soft tissue could also affect the instantaneous curvature at the tip, but we have experimentally observed that curvature is independent of depth (see Figs. 9 and 14 for example). This would seem to suggest a seven-dimensional space required to characterize the curvature of our needle: $\kappa = f(I, E, L, D, \tau, E_{st}, \nu_{st})$. However, these eight variables (one dependent and seven independent) comprise two distinct dimensions (m and N; see Table I), so the Buckingham Π theorem [62], [63] tells us that the physics of interest can be described by at most $8 - 2 = 6$ variables (*i.e.*, one dependent and five independent) using dimensionless Π groups: $\Pi_0 = f(\Pi_1, \Pi_2, \Pi_3, \Pi_4, \Pi_5)$. These Π groups are not unique, but we have provided a valid set in Table I in which we have used I to nondimensionalize with respect to the dimension m, and E to nondimensionalize with respect to the dimension N independently from the dimension m. The result can be thought of as a nondimensional curvature Π_0 that is a function of: a nondimensional magnetic-screw length, Π_1; a nondimensional magnetic-screw diameter, Π_2; a nondimensional applied torque, Π_3; a nondimensional soft-tissue modulus of elasticity, Π_4; and the already nondimensional Poisson's ratio of the soft-tissue, Π_5. The Buckingham Π theorem does not tell us anything about the form of the resulting function, but these nondimensional groups will enable us to elegantly and efficiently characterize the steerability of our needles empirically.

TABLE I
Instantaneous Curvature κ and the Seven Independent Parameters That May Affect it, Shown in Dimensional and Nondimensional Forms

Parameter	Units	Π group
κ	m^{-1}	$\Pi_0 = \kappa I^{1/4}$
I	m^4	
E	$\mathrm{N{\cdot}m}^{-2}$	
L	m	$\Pi_1 = LI^{-1/4}$
D	m	$\Pi_2 = DI^{-1/4}$
τ	N·m	$\Pi_3 = \tau E^{-1} I^{-3/4}$
E_{st}	$\mathrm{N{\cdot}m}^{-2}$	$\Pi_4 = E_{st} E^{-1}$
ν_{st}	—	$\Pi_5 = \nu_{st}$

Since Π_5 is purely a function of the soft tissue in which the needle is being steered, we would only be interested in values of Π_5 that correspond to specific soft-tissues of clinical interest for a specific application (for which $\Pi_5 \approx 0.5$); this reduces the independent parameters from five to four for a given soft tissue. Once a material has been identified for the compliant tube, Π_4 becomes constant for a specific soft tissue, which would further reduce the independent parameters from four to three: $\Pi_0 = f(\Pi_1, \Pi_2, \Pi_3)$.

It is worth noting that in the absence of any soft tissue, in which $\Pi_4 = 0$ and Π_5 is undefined, the torque applied anywhere on the rigid magnetic-screw tip will be transferred to the distal end of the compliant tube such that L and D, and thus Π_1 and Π_2, have no bearing on the curvature. In this case, the nondimensional relationship simplifies to $\Pi_0 = f(\Pi_3)$. We know that an empirical characterization of this function would reveal that it is linear with a slope of 1, which would in turn lead to the well-known formula for the constant curvature of a cantilever beam with an applied torque (*i.e.*, applied moment) at its end:

$$\kappa I^{1/4} = \frac{\tau}{EI^{3/4}} \quad \Rightarrow \quad \kappa = \frac{\tau}{EI} \tag{5}$$

It is based on this consideration that we believe that our choice of Π groups, although not unique, is well-founded. The curvature of (5) is an upper bound on the achievable curvature for a given needle and applied torque in a given soft tissue. We expect the presence of soft tissue to reduce the actual curvature below this upper bound.

TABLE II
PHYSICAL AND NONDIMENSIONAL PARAMETERS OF EACH NEEDLE USED IN CURVATURE CHARACTERIZATION

Needle	L [mm]	D [mm]	Π_1	Π_2
Fig. 4(c)	3.0	1	8.4	2.8
Fig. 4(d)	4.3	1	12	2.8
Fig. 4(e)	5.7	1	15.7	2.8
Fig. 4(f)	4.3	1.5	12	4.2

B. Experiments

We performed experiments to characterize the effects of Π_1, Π_2, Π_3, and Π_4 on the nondimensional curvature Π_0. Given our focus on brain tissue in this work, in the experiments that follow, Π_5 is fixed during the exploration. The Tygon tubing of our needles has an area moment of inertia $I = 0.016\,\text{mm}^4$ and modulus of elasticity $E = 8.6\,\text{MPa}$. To measure E, we performed a standard tensile test on an Instron 5943 and a linear model was fit to the recorded stress-strain data up to 5% strain.

Three needles with $L \in \{3.0,\ 4.3,\ 5.7\}\,\text{mm}$ and $D = 1\,\text{mm}$ (Figs. 4(c)–4(e)), representing $\Pi_1 \in \{8.4,\ 12,\ 15.7\}$ with $\Pi_2 = 2.8$, were used to characterize how Π_0 is affected by Π_1 and Π_3 for fixed Π_2 and Π_4. Then, a fourth needle with $L = 4.3\,\text{mm}$ and $D = 1.5\,\text{mm}$ (Fig. 4(f)), representing $\Pi_1 = 12$ and $\Pi_2 = 4.2$, was used to characterize how Π_2 affects Π_0 independently of the other three terms. These needle parameters are summarized in Table II.

Three concentrations of agar gel were used to characterize how Π_0 is affected by Π_3 and Π_4 for fixed Π_1 and Π_2. The modulus of elasticity for each of these agar concentrations—0.325 wt%, 0.5 wt%, and 0.625 wt%—was measured to be $E_{st} \in \{1.9, 4.6, 9.3\}\,\text{kPa}$, respectively (which agrees with previously published results [58]). E_{st} was measured on an Instron 5943 using a standard compression test with 17.5 mm diameter cylindrical samples and a linear fit to the recorded stress-strain data up to 15% strain. The Poisson's ratio of our agar gel recipe is $\nu_{st} = \Pi_5 = 0.5$. These physical properties result in $\Pi_4 \in \{2.2 \times 10^{-4}, 5.3 \times 10^{-4}, 1.1 \times 10^{-3}\}$.

Each needle was inserted into the 0.5 wt% agar gel concentration five times at three different torques $\tau \in \{0.1479 \times 10^{-3},\ 0.1208 \times 10^{-3},\ 0.93738 \times 10^{-4}\}$ N·m (and thus three different values of Π_3), totaling 15 insertions per needle, and the resulting curvature was recorded. The needle of Fig. 4(d) was also inserted into the other two agar concentrations five times at the same three torques totaling 30 additional insertions with that needle. Each insertion comprised a 15 mm straight section (*i.e.*, no applied torque) followed by constant applied torque until either the needle completed a quarter circle or the full stroke of our insertion device was reached. The results, presented as 95% confidence intervals on the mean of five insertions, are shown in Figs. 11–13.

C. Empirical Model

We used linear-regression techniques to fit a parsimonious model to the data described above. Such a model can be used for motion planners and predictive feed-forward terms in closed-loop trajectory-tracking controllers, as a guide for needle design, and for future feasibility studies for specific applications.

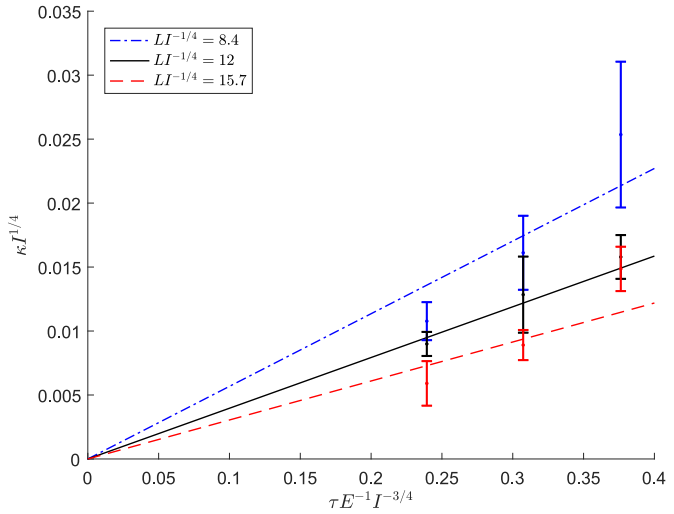

Fig. 11. Nondimensional curvature Π_0 as a function of nondimensional torque Π_3 for three different values of nondimensional length Π_1, with $\Pi_2 = 2.8$, $\Pi_4 = 5.3 \times 10^{-4}$, and $\Pi_5 = 0.5$. Error bars depict 95% confidence intervals on the means ($n = 5$). Curves depict results of parsimonious regression model.

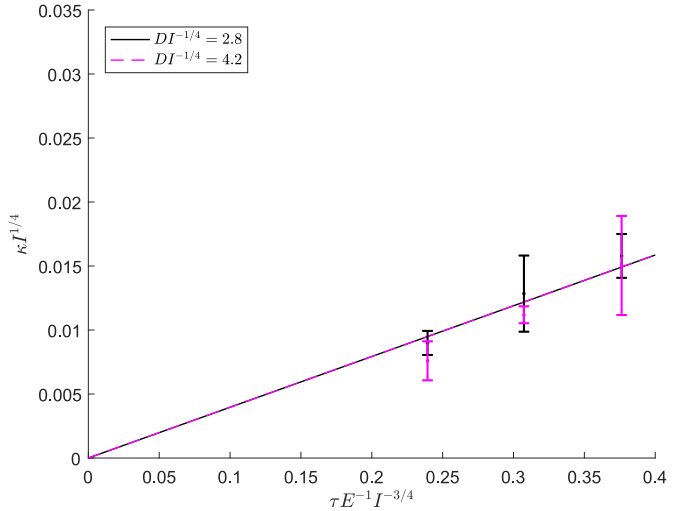

Fig. 12. Nondimensional curvature Π_0 as a function of nondimensional torque Π_3 for two different values of nondimensional diameter Π_2, with $\Pi_1 = 12$, $\Pi_4 = 5.3 \times 10^{-4}$, and $\Pi_5 = 0.5$. Error bars depict 95% confidence intervals on the means ($n = 5$). Curves depict results of parsimonious regression model.

We started our model fitting by observing that, in our data, Π_0 is approximately linear with respect to Π_3 with all other parameters fixed (noting that, from first principles, $\Pi_0 = 0$ when $\Pi_3 = 0$). We also observed that Π_0 is insensitive to Π_2 (at least for the values of Π_2 that we considered). This suggests a model of the form $\Pi_0 = c_0(\Pi_1, \Pi_4)\Pi_3$, where the coefficient c_0 is a function of Π_1 and Π_4. Next, we observed that, in our data, Π_0 is approximately linear with respect to Π_1^{-1} with all other parameters fixed (although we only explicitly considered $\Pi_4 > 0$). In addition, as discussed in Section VI-A, our model should give $\Pi_0 = \Pi_3$ when $\Pi_4 = 0$. In order to achieve these constraints, we used a generalized logistic function for

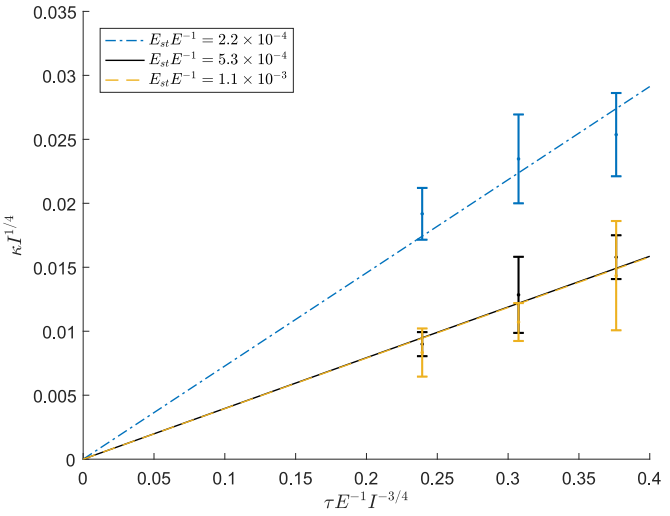

Fig. 13. Nondimensional curvature Π_0 as a function of nondimensional torque Π_3 for three different values of nondimensional soft tissue modulus of elasticity Π_4, with $\Pi_1 = 12$, $\Pi_2 = 2.8$, and $\Pi_5 = 0.5$. Error bars depict 95% confidence intervals on the means ($n = 5$). Curves depict results of parsimonious regression model.

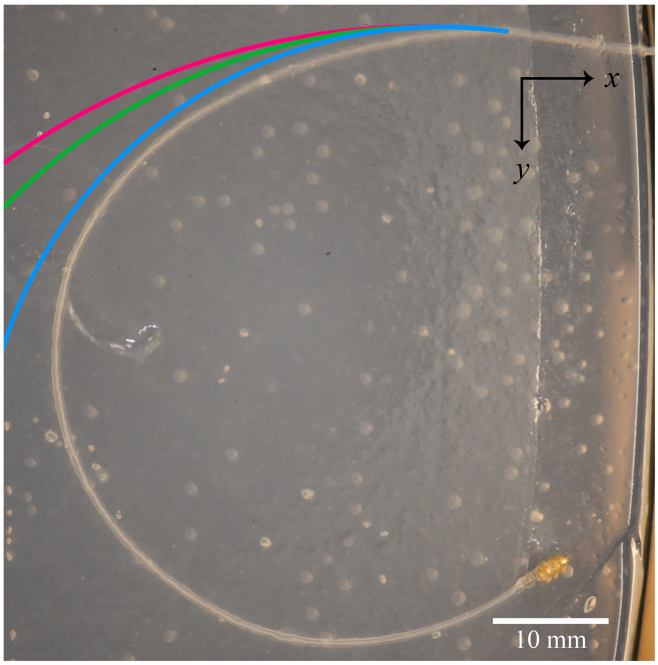

Fig. 14. Typical curvature achieved in brain-simulating gel phantom for our needle with a functional lumen (the needle from Fig. 4(a)). After an initial unsteered (straight) insertion of 14 mm, our needle was steered with approximately constant torque to achieve an RoC of 29.0 mm, with an insertion depth of 144 mm and a total turn of 210°. We compare our results to three state-of-the-art results, depicted tangent to the straight portion at the point where our steering began: the pink curve depicts a 61.8 mm RoC, which was obtained in brain in [8]; the green curve depicts a 52.1 mm RoC, which was obtained in brain-simulating gel phantom in [64]; the blue curve depicts a 40.3 mm RoC, which was obtained in brain in [43].

$c_0(\Pi_1, \Pi_4)$, with two free coefficients. The result is a final parsimonious nondimensional model of curvature:

$$\Pi_0 = \left(\frac{c_1}{\Pi_1} + \frac{2 - \frac{c_1}{\Pi_1}}{1 + \left(\frac{\Pi_1}{\Pi_1 - c_1} \right) e^{c_2 \Pi_4}} \right) \Pi_3 \tag{6}$$

Using regression, we arrived at the coefficients $c_1 = 0.48$ and $c_2 = 1.80 \times 10^4$ with an adjusted $R^2 = 0.74$. This model is depicted in Figs. 11–13; it is clear that this simple, two-parameter model is capturing the essential behavior of our steerable needle. We can recast (6) back in terms of curvature directly:

$$\kappa = \left(\frac{c_1}{LEI^{3/4}} + \frac{\frac{2}{EI} - \frac{c_1}{LEI^{3/4}}}{1 + \left(\frac{L}{L - c_1 I^{1/4}} \right) e^{c_2 \frac{E_{st}}{E}}} \right) \tau, \tag{7}$$

where units should be consistent with Table I.

This model then serves as a guiding fit for what curvatures will be achievable for a given needle design and tissue, including needles that have never been tested, with a given applied magnetic torque. During real-time control, τ is the only control variable, with all other parameters fixed by the tissue and the needle design.

VII. Comparison to Existing Steerable Needles

We compare our needle design to existing steerable needles using values reported in the literature as well as values obtained with physical instantiations of other needle designs.

We first compare curvature values achievable by the prototype with a functional lumen (Fig. 4(a)) to that reported in the literature for existing steerable needles. We first inserted the needle straight (*i.e.*, with no steering) into 0.5 wt% agar to an insertion depth of at least 10 mm to establish a straight heading and reduce the effects of any misalignment at insertion (note that this is just an experimental detail, the needle could begin curving at any location). Next, we steered with $\|\boldsymbol{p}\| = 45$ mm and $|\theta| = 90°$, which results in an approximately constant torque of 9.6×10^{-5} N·m. A typical resulting steer is provided in Fig. 14, in which the needle achieved an RoC of 29.0 mm and a total insertion depth of 144 mm. Notably, we were able to turn the needle through an angle of 210° measured from initial heading to the final heading, whereas prior designs have struggled to go beyond 90° without tissue damage. We note that we terminated this steer when the screw tip reached the upper surface of the phantom, as we are not controlling the vertical position in our experiments, and we believe we could have gone farther with a different experimental design. Fig. 14 also depicts the curvature of three state-of-the-art results which had RoC's of 61.8 mm [8], 52.1 mm [64], and 40.3 mm [43] (see more discussion of this final comparison in Section VIII).

Next, we compare the curvature achieved by the prototype of Fig. 4(d) in the three agar concentrations of Section VI (*i.e.*, all of the data presented in Fig. 13) to that achieved by three existing steerable-needle designs inserted into those same agar concentrations. The three existing steerable-needle designs, depicted in Fig. 15, are a helical dovetail laser-patterned needle with a flexure hinge [8], a standard bevel-tip needle [24], and a kinked-tip needle [25]. The dovetail needle has a diameter of 1.28 mm. The bevel-tip and kinked-tip needles have head diameters of 1.2 mm and 1 mm, respectively, and both have a shaft diameter of 0.35 mm. The needles are all made

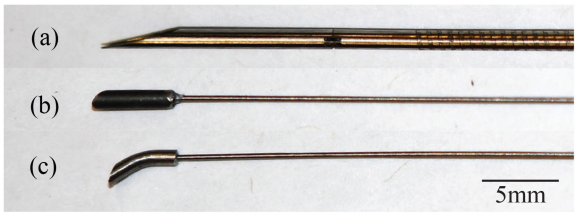

Fig. 15. Images of existing steerable needles used for comparison. (a) Helical dovetail laser-patterned needle with flexure hinge [8]. (b) Standard bevel-tip needle with larger head [24]. (c) Kinked-tip needle with larger head [25].

TABLE III
p-VALUES COMPARING κ ACHIEVED BY EXISTING STEERABLE NEEDLES TO κ ACHIEVED BY OUR STEERABLE NEEDLE AT AN APPLIED TORQUE $\tau = 9.4 \times 10^{-5}$ N · m, IN TISSUE PHANTOMS OF VARYING STIFFNESS E_{st}

E_{st} [Pa]	1925	4592	9311
Dovetail	2.1×10^{-7}	2.1×10^{-6}	1.2×10^{-3}
Bevel-tip	2.2×10^{-7}	5.0×10^{-5}	0.071
Kinked-tip	2.8×10^{-7}	2.3×10^{-5}	0.049

TABLE IV
p-VALUES COMPARING ROC ACHIEVED BY EXISTING STEERABLE NEEDLES TO ROC ACHIEVED BY OUR STEERABLE NEEDLE AT AN APPLIED TORQUE $\tau = 9.4 \times 10^{-5}$ N · m, IN TISSUE PHANTOMS OF VARYING STIFFNESS E_{st}

E_{st} [Pa]	1925	4592	9311
Dovetail	1.4×10^{-11}	2.6×10^{-6}	3.0×10^{-6}
Bevel-tip	2.5×10^{-9}	1.0×10^{-5}	0.030
Kinked-tip	1.9×10^{-6}	3.1×10^{-5}	0.019

of Nitinol except the head of the kinked-tip needle, which is made of aluminum. These needles were inserted 5 times into each concentration, by hand, through a fixed stabilizing aluminum tube and were not rotated such that the maximum curvature was achieved.

The results of these trials compared to the screw-tip needle are presented in Fig. 16. Results are presented in terms of both curvature and RoC, since both metrics are commonly used in the literature. Figure 16 shows that our needle performs better than these competing needle designs in these phantoms. A clear contrast of our screw-tip needle compared to existing steerable needles, revealed by Fig. 16, is that resulting curvature decreases as tissue stiffness increases with our needle whereas the opposite is true for the other needles. We expect this would also be true for any magnetically steered needle.

Tables III and IV present *p*-values from two-sample *t*-tests comparing the steerability of each existing needle design to the poorest performance of our needle—*i.e.*, at the weakest evaluated applied torque ($\tau = 9.4 \times 10^{-5}$ N · m)—in each of the three tissue phantoms of varying stiffness. These statistical results further emphasize the trade-off between existing needle designs and our design with respect to tissue stiffness, *i.e.*, that as tissue stiffness decreases, the steerability of our needle increases relative to existing designs.

VIII. DISCUSSION

The key insight to our new concept is that the tube can be extremely flexible and still transmit rotation to its tip, particularly when that rotation is in a sustained direction, as is

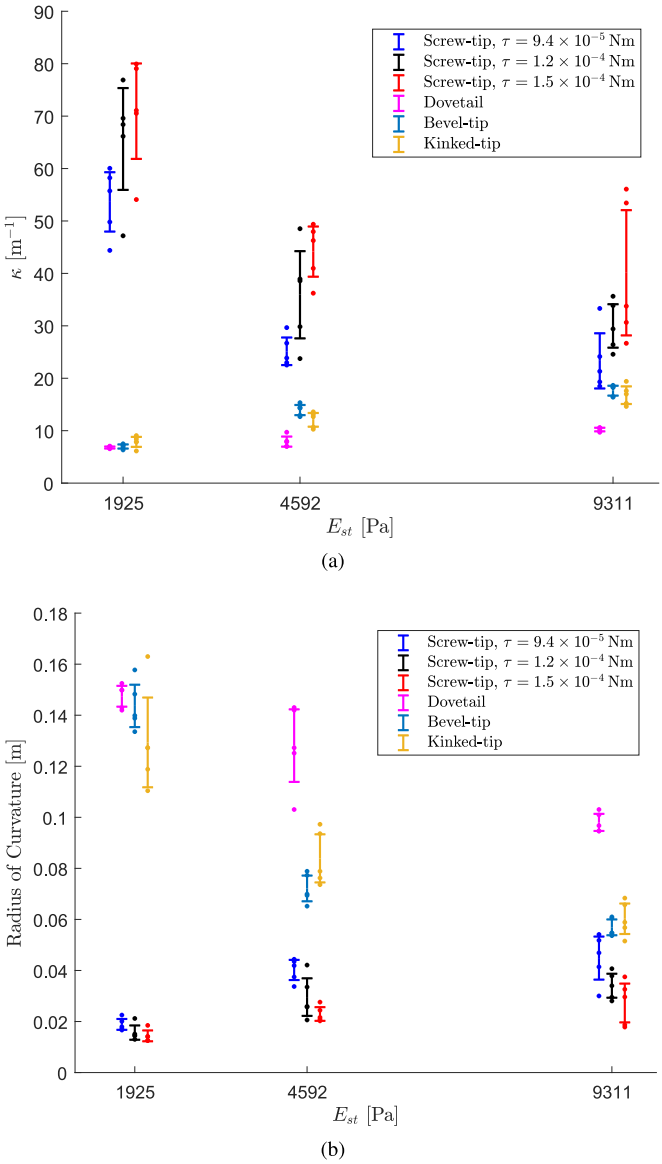

Fig. 16. We compare turning capabilities of our needle at three magnetic torque values against three competing needle types in three agar-based tissue phantoms with varying stiffness. We show the same data as both (a) curvature, and (b) RoC. Dots represent individual trials and error bars depict 95% confidence intervals on the means ($n = 5$).

the case with our design. This enables one of the key benefits to our design over existing designs, which was previously noted in [46]: as the tube is not required to transmit an axial force from its base to its tip, *i.e.*, be pushed from behind, our design leverages a much more flexible tube than other existing designs. This has two benefits: (i) it reduces the stress the needle imparts on surrounding tissue, as the tissue is not being tasked with maintaining a curve on a semi-rigid tube, and (ii) the more flexible tube enables tighter curvature values during steering. Our results also demonstrate the potential of this needle design to precisely navigate with high curvature to a particular region of interest in the brain for targeted therapies such as energy-based ablation. They further demonstrate an ability to take branching paths when necessary, potentially enabling complete coverage of a region while minimizing travel through healthy tissue.

These benefits are demonstrated in Fig. 14 where our design pulls itself through a circular arc with far more arc length than is typically achievable without tissue damage, while also exhibiting tighter curvature than state-of-the-art designs. We note that, in the system described in [42], [43], they report a minimum RoC in brain-mimicking gel phantom of "100 mm without inducing tissue damage and down to 30 mm if some tissue damage is tolerable" (with damage similar to lateral cutting reported elsewhere in the literature [8], but due to shearing of their kinked tip), using an 80 mT field. They also report achieving a 40.3 mm RoC in brain, using a 60 mT field. Since it is not clear what a tolerable amount of damage is, we chose to include the 40.3 mm RoC for comparison.

Although the total turning angles and curve shapes demonstrated in Figs. 9 and 14 are not necessarily required for the epilepsy ablation case discussed in this paper, we note that we expect our design to be potentially useful for a variety of clinical uses both anticipated (*e.g.*, targeted therapy or biopsy of tumors) and unanticipated. As such, we seek to characterize the performance of our design broadly.

It is important to note that steering based on magnetism is proportional to the achievable magnetic torque. This is unlike steering based on tip geometry. As such, the curvatures that we have reported in this paper should not be viewed as the best achievable, but rather, the (approximately) best achievable using our functional-prototype needles and benchtop SAMM system. For instance, due to the geometry of the *ex vivo* brain, we were only able to get the SAMM to a height of 55 mm above the needle tip, as opposed to the 45 mm used in the gel-phantom demonstrations. This produces a weaker field (*i.e.*, fields of 39.7 mT at 55 mm, compared to 72.4 mT at 45 mm), and thus a 45% smaller torque than that used in the gel-phantom trials. As a result, direct comparison with the results in the gel phantom should be made with caution. Regardless of the reason, the fact that the actual path taken was different from the expected (open-loop) path indicates that the steering was suboptimal (*i.e.*, the steering angle θ was different than 90°), which suggests that a tighter curvature could have been achieved through closed-loop control (although the magnitude of the improvement is unknown).

Our results show that our design achieves tighter curvature in softer tissues than stiffer ones, as opposed to traditional steerable needles that have been shown to do the opposite [8]. Indeed, the results of Fig. 16 suggest that our needle is best suited to delicate tissues and more traditional needles are better suited to stiffer tissues.

Absent from this work is a treatment of the potential excess damage that adding threads to the tip of a steerable needle might cause as it passes through delicate tissues. A quantitative approach to thinking about damage could be to consider damage equal to the circumference of the resulting hole integrated over the length of the insertion. Our needles could then be compared in terms of damage potential by inserting threaded needles and comparably sized smooth needles (*i.e.*, the threaded needle minor diameter matches the smooth needle OD) into fresh tissue and measuring the resulting hole circumference. In the limit as the thread height of the threaded needle reaches zero, we would expect resulting damage to converge on that of the smooth needle. The materials used for the various parts of our steerable needles may also play a significant role in the amount of excess damage. Indeed, low-friction biocompatible materials should be used, perhaps with surface properties similar to that of medical-grade stainless steels used for clinical needles.

The addition of the lumen in the screw has the effect of removing the most distal (*i.e.*, sharpest) portion of the tip of the screw. Although we did not observe any problem related to this effect in our study, it is possible it could become problematic if the lumen becomes too large relative to the major/minor diameters of the screw. A related concern is tissue coring. We observed no coring for any of our designs in gel or *ex vivo* brain, but we anticipate that coring may eventually occur if the lumen size is increased.

Although we expect tissue damage from our screw tip to be locally greater than that of some current needles, we expect the ability to take safer and/or shorter paths enabled by our needle will reduce damage overall for certain applications. As noted by Pinzi et al. [21], the ability to take expressive paths enables access to targets via safer insertion trajectories and the ability to provide targeted treatment that damages less healthy tissue while increasing the efficacy of the treatment. With this in mind, the notion of damage from a broader perspective needs to be quantified and analyzed for our device, which is left as an open problem.

In the consideration of reducing the height of the threads in our design, there exists a trade-off between damage reduction and the achievable insertion depth. As the insertion depth increases, so does friction, which may cause the needle to 'strip' or drill rather than advance. One of the major limiting factors of steerable needles is the maximum achievable depth. For the maximum-curvature experiment shown in Fig. 14, we maintained a tight curvature over 130 mm of insertion, after an initial nearly straight insertion of approximately 14 mm (*i.e.*, a total insertion of 144 mm), but again, our steer was terminated when the screw tip reached the upper surface of the phantom (not representing its depth limit). However, in the steer of Fig. 9(a) the needle did reach a maximum insertion depth of 65 mm due to the tube twisting described previously. We also performed several insertions with all our needle prototypes along an approximately straight path (*i.e.*, no steering), and the needles were able to traverse the entire 200 mm length of a gel phantom before exiting the phantom, so even greater depth may have been achievable. These results are promising for applications in the brain, given that the length of the average human brain is approximately 150 mm [61]. We believe that insertion depth will be a function of the thread geometry and the trajectory.

With our system—in which we are relying on magnetic torque for actuation, generated by a permanent-magnet field source—the scaling analysis is straightforward due to the homothetic property of magnetic fields [45]: if the radius ρ (units m) of the original external magnet were increased by a factor of k, then the field, and thus torque, measured at $k\boldsymbol{p}$ would be the same as that measured at $\boldsymbol{p}$ with the original magnet. In this paper, our experiments were performed at nondimensional distances $\|\boldsymbol{p}\|/\rho$ in the range of 1.7–2.6, and

we should expect the same performance at the same nondimensional distances as we scale up our external magnet in a clinical system. It is worth noting that techniques relying on magnetic force (*e.g.*, [46]) scale $\propto 1/k$ at distances of $k\boldsymbol{p}$.

In this study, we limited our experiments to a special configuration in which the applied magnetic force is prescribed to have zero magnitude. In reality, this constraint is artificially limiting—attempting to drive the applied force to zero is not necessarily the best strategy and it may be advantageous to apply forward force to the needle tip. Steering of our needle via applied magnetic torque only requires 2-DOF magnetic actuation. There exist many suitable magnetic actuation systems, with varying workspace size, capable of applying arbitrary torque to a magnet with arbitrary pose [45]. Our choice to actuate using a single mobile external permanent magnet results in a 5-DOF input space and thus a 3-DOF null space imparting redundancy in the pose of the external magnet. The greatest priority in utilizing this redundancy will be to eliminate workspace collisions; however, additional objectives can be taken into consideration such as external magnet trajectory smoothness or optimizing the applied magnetic force, the choice for which may be problem specific. This is left as an open problem.

Closed-loop magnetic steering requires knowledge of the 5-DOF pose of the needle's tip (*i.e.*, 3-DOF position and 2-DOF pointing orientation). Due to the limitations of our experimental setup we had to assume planar motion and localization. In reality, the needle tip was free to pitch upward or downward, allowing the potential for out-of-plane trajectories. This manifests as uncertainty in the applied torque, however, the thin agar phantoms bound this uncertainty by preventing out-of-plane motion beyond approximately 5 mm in either direction. We believe that this uncertainty in applied torque is a primary factor contributing to the variance between trials and the resulting size of the confidence intervals in Figs. 11–13 and 16, and we anticipate less variance from a system capable of 5-DOF needle pose estimation and closed-loop torque control. These problems all stem from the need to use computer vision for localization given the higher complexity of localization without line-of-sight. To further evaluate the performance of this needle in opaque tissues (such as the brain) with 3D regions of interest, closed-loop control and localization without line-of-sight is required. Such localization can be achieved through medical-imaging or potentially through magnetic localization. Such 3D, closed-loop control requires localization, trajectory planning, and a robust and effective controller. The development of an integrated system of this type is left as an open problem.

We note that, because we use permanent magnets on the tip of our needle, our system is not MRI compatible. However, many cases of ablation-based epilepsy treatment, such as we describe in this paper, are performed via RF-ablation without MRI-based monitoring during ablation [17], [18], [19]. Further, we envision many potential clinical applications that can be performed with our device under localization via other, non-magnetic imaging modalities. Such modalities include mono- or biplane fluoroscopy, intermittent multi-view X-ray, CT, or ultrasound. For many applications, our system will need to be integrated with such imaging. The co-location of the robotically actuated steering magnet of our system and the imaging modality will depend on the specific imaging technique, however we note that our current system steers sufficiently slowly such that imaging can be interleaved with steering.

The steerable needle concept presented here represents a new class of needle aimed at applications in delicate tissue. The analysis provides both characterization of our prototypes of the design—demonstrating significant steerability—as well as a model that informs future instantiations of the design. We believe that the design and model lay the groundwork for future clinically relevant targeted therapy and biopsy in delicate tissues with the potential to improve patient outcomes.

ACKNOWLEDGMENT

The authors thank Shervin Rahimpour, MD for providing us with a DBS cannula. They also thank the anonymous reviewers, whose comments helped improve this paper.

REFERENCES

[1] R. J. Webster, III, J. S. Kim, N. J. Cowan, G. S. Chirikjian, and A. M. Okamura, "Nonholonomic modeling of needle steering," *Int. J. Robot. Res.*, vol. 25, nos. 5–6, pp. 509–525, May 2006.

[2] N. Abolhassani, R. Patel, and M. Moallem, "Needle insertion into soft tissue: A survey," *Med. Eng. Phys.*, vol. 29, no. 4, pp. 413–431, May 2007.

[3] K. B. Reed et al., "Robot-assisted needle steering," *IEEE Robot. Autom. Mag.*, vol. 18, no. 4, pp. 35–46, Dec. 2011.

[4] P. J. Swaney et al., "Toward transoral peripheral lung access: Combining continuum robots and steerable needles," *J. Med. Robot. Res.*, vol. 2, no. 1, Mar. 2021, Art. no. 1750001.

[5] A. Majewicz et al., "Behavior of tip-steerable needles in ex vivo and in vivo tissue," *IEEE Trans. Biomed. Eng.*, vol. 59, no. 10, pp. 2705–2715, Oct. 2012.

[6] R. Alterovitz, K. Goldberg, and A. M. Okamura, "Planning for steerable bevel-tip needle insertion through 2D soft tissue with obstacles," in *Proc. IEEE Int. Conf. Robot. Autom.*, Apr. 2005, pp. 1652–1657.

[7] D. Minhas, J. A. Engh, and C. N. Riviere, "Testing of neurosurgical needle steering via duty-cycled spinning in brain tissue in vitro," in *Proc. Annu. Int. Conf. IEEE EMBS*, Sep. 2009, pp. 258–261.

[8] M. Rox et al., "Decoupling steerability from diameter: Helical dovetail laser patterning for steerable needles," *IEEE Access*, vol. 8, pp. 181411–181419, 2020.

[9] O. Ashraf, N. V. Patel, S. Hanft, and S. F. Danish, "Laser-induced thermal therapy in neuro-oncology: A review," *World Neurosurg.*, vol. 112, pp. 166–177, Apr. 2018.

[10] M. Riche, A. Amelot, M. Peyre, L. Capelle, A. Carpentier, and B. Mathon, "Complications after frame-based stereotactic brain biopsy: A systematic review," *Neurosurg. Rev.*, vol. 44, no. 1, pp. 301–307, Feb. 2021.

[11] M. A. Vogelbaum and M. K. Aghi, "Convection-enhanced delivery for the treatment of glioblastoma," *Neuro Oncol.*, vol. 17, no. S2, pp. ii3–ii8, Mar. 2015.

[12] S. Shimamoto, C. Wu, and M. R. Sperling, "Laser interstitial thermal therapy in drug-resistant epilepsy," *Curr. Opin. Neurol.*, vol. 32, no. 2, pp. 237–245, Apr. 2019.

[13] J. Voges, L. Büntjen, and F. C. Schmitt, "Radiofrequency-thermoablation: General principle, historical overview and modern applications for epilepsy," *Epilepsy Res.*, vol. 142, pp. 113–116, May 2018.

[14] R. R. Lonser, A. S. Akhter, M. Zabek, J. B. Elder, and K. S. Bankiewicz, "Direct convective delivery of adeno-associated virus gene therapy for treatment of neurological disorders," *J. Neurosurg.*, vol. 134, no. 6, pp. 1751–1763, 2020.

[15] H. J. Marcus et al., "Computer-assisted versus manual planning for stereotactic brain biopsy: A retrospective comparative pilot study," *Oper. Neurosurg.*, vol. 18, no. 4, pp. 417–422, Apr. 2020.

[16] M. Cossu, L. Mirandola, and L. Tassi, "RF-ablation in periventricular heterotopia-related epilepsy," *Epilepsy Res.*, vol. 142, pp. 121–125, May 2018.

[17] L. Mirandola et al., "Stereo-EEG: Diagnostic and therapeutic tool for periventricular nodular heterotopia epilepsies," *Epilepsia*, vol. 58, no. 11, pp. 1962–1971, Nov. 2017.

[18] D. Wang, P. Wei, Y. Shan, L. Ren, Y. Wang, and G. Zhao, "Optimized stereoelectroencephalography-guided radiofrequency thermocoagulation in the treatment of patients with focal epilepsy," *Ann. Transl. Med.*, vol. 8, no. 1, p. 15, Jan. 2020.

[19] N. G. Losarcos et al., "Stereotactic-EEG-guided radiofrequency multiple hippocampal transection (SEEG-guided-RF-MHT) for the treatment of mesial temporal lobe epilepsy: A minimally invasive method for diagnosis and treatment," *Epileptic Disord.*, vol. 23, no. 5, pp. 682–694, Oct. 2021.

[20] S. S. Grewal et al., "Laser ablation for mesial temporal epilepsy: A multi-site, single institutional series," *J. Neurosurg.*, vol. 130, pp. 2055–2062, Jul. 2018.

[21] M. Pinzi, V. N. Vakharia, B. Y. Hwang, W. S. Anderson, J. S. Duncan, and F. R. Y. Baena, "Computer assisted planning for curved laser interstitial thermal therapy," *IEEE Trans. Biomed. Eng.*, vol. 68, no. 10, pp. 2957–2964, Oct. 2021.

[22] T. J. Schwehr, A. J. Sperry, J. D. Rolston, M. D. Alexander, J. J. Abbott, and A. Kuntz, "Toward targeted therapy in the brain by leveraging screw-tip soft magnetically steerable needles," in *Proc. Hamlyn Symp. Med. Robot.*, 2022, pp. 81–82.

[23] N. J. van de Berg, D. J. van Gerwen, J. Dankelman, and J. J. van den Dobbelsteen, "Design choices in needle steering—A review," *IEEE/ASME Trans. Mechatronics*, vol. 20, no. 5, pp. 2172–2183, Oct. 2015.

[24] R. J. Webster, III, J. Memisevic, and A. M. Okamura, "Design considerations for robotic needle steering," in *Proc. IEEE Int. Conf. Robot. Autom.*, Apr. 2005, pp. 3599–3605.

[25] J. A. Engh, G. Podnar, D. Kondziolka, and C. N. Riviere, "Toward effective needle steering in brain tissue," in *Proc. IEEE EMBS Annu. Int. Conf.*, Sep. 2006, pp. 559–562.

[26] P. J. Swaney, J. Burgner, H. B. Gilbert, and R. J. Webster, III, "A flexure-based steerable needle: High curvature with reduced tissue damage," *IEEE Trans. Biomed. Eng.*, vol. 60, no. 4, pp. 906–909, Apr. 2013.

[27] S. Okazawa, R. Ebrahimi, J. Chuang, S. E. Salcudean, and R. Rohling, "Hand-held steerable needle device," *IEEE/ASME Trans. Mechatronics*, vol. 10, no. 3, pp. 285–296, Jun. 2005.

[28] H. B. Gilbert, J. Neimat, and R. J. Webster, "Concentric tube robots as steerable needles: Achieving follow-the-leader deployment," *IEEE Trans. Robot.*, vol. 31, no. 2, pp. 246–258, Apr. 2015.

[29] F. Yang, M. Babaiasl, and J. P. Swensen, "Fracture-directed steerable needles," *J. Med. Robot. Res.*, vol. 4, no. 1, Mar. 2018, Art. no. 1842002.

[30] E. Matheson and F. R. Y. Baena, "Biologically inspired surgical needle steering: Technology and application of the programmable bevel-tip needle," *Biomimetics*, vol. 5, no. 4, p. 68, 2020.

[31] R. Secoli et al., "Modular robotic platform for precision neurosurgery with a bio-inspired needle: System overview and first in-vivo deployment," *PLoS One*, vol. 17, Oct. 2022, Art. no. e0275686.

[32] J. Bloemberg, F. Trauzettel, B. Coolen, D. Dodou, and P. Breedveld, "Design and evaluation of an MRI-ready, self-propelled needle for prostate interventions," *PLoS One*, vol. 17, Sep. 2022, Art. no. e0274063.

[33] N. J. van de Berg, J. Dankelman, and J. J. van den Dobbelsteen, "Design of an actively controlled steerable needle with tendon actuation and FBG-based shape sensing," *Med. Eng. Phys.*, vol. 37, no. 6, pp. 617–622, 2015.

[34] G. Gerboni, J. D. Greer, P. F. Laeseke, G. L. Hwang, and A. M. Okamura, "Highly articulated robotic needle achieves distributed ablation of liver tissue," *IEEE Robot. Autom. Lett.*, vol. 2, no. 3, pp. 1367–1374, Jul. 2017.

[35] S. C. Ryu, Z. F. Quek, P. Renaud, R. J. Black, B. L. Daniel, and M. R. Cutkosky, "An optical actuation system and curvature sensor for a MR-compatible active needle," in *Proc. IEEE Int. Conf. Robot. Autom.*, 2012, pp. 1589–1594.

[36] A. Yamada, S. Naka, N. Nitta, S. Morikawa, and T. Tani, "A loop-shaped flexible mechanism for robotic needle steering," *IEEE Robot. Autom. Lett.*, vol. 3, no. 2, pp. 648–655, Apr. 2018.

[37] A. Yamada, N. Nitta, S. Naka, K. T. Dang, S. Morikawa, and T. Tani, "Design and implementation of loop shaped steering mechanisms for flexible needles," in *Proc. Int. Conf. Develop. Biomed. Eng. Vietnam*, 2018, pp. 15–19.

[38] D. C. Rucker and R. J. Webster, III, "Statics and dynamics of continuum robots with general tendon routing and external loading," *IEEE Trans. Robot.*, vol. 27, no. 6, pp. 1033–1044, Dec. 2011.

[39] P. E. Dupont, J. Lock, B. Itkowitz, and E. Butler, "Design and control of concentric-tube robots," *IEEE Trans. Robot.*, vol. 26, no. 2, pp. 209–225, Apr. 2010.

[40] H. B. Gilbert, D. C. Rucker, and R. J. Webster, III, "Concentric tube robots: The state of the art and future directions," in *Robotics Research*. Cham, Switzerland: Springer, 2016, pp. 253–269.

[41] J. Burgner-Kahrs, D. C. Rucker, and H. Choset, "Continuum robots for medical applications: A survey," *IEEE Trans. Robot.*, vol. 31, no. 6, pp. 1261–1280, Dec. 2015.

[42] A. J. Petruska et al., "Magnetic needle guidance for neurosurgery: Initial design and proof of concept," in *Proc. IEEE Int. Conf. Robot. Autom.*, 2016, pp. 4392–4397.

[43] A. Hong, A. J. Petruska, A. Zemmar, and B. J. Nelson, "Magnetic control of a flexible needle in neurosurgery," *IEEE Trans. Biomed. Eng.*, vol. 68, no. 2, pp. 616–627, Feb. 2021.

[44] X. Hu, A. Chen, Y. Luo, C. Zhang, and E. Zhang, "Steerable catheters for minimally invasive surgery: A review and future directions," *Comput. Assist. Surg.*, vol. 23, pp. 21–41, Dec. 2018.

[45] J. J. Abbott, E. Diller, and A. J. Petruska, "Magnetic methods in robotics," *Annu. Rev. Control Robot. Auton. Syst.*, vol. 3, pp. 57–90, May 2020.

[46] M. Ilami, R. J. Ahmed, A. Petras, B. Beigzadeh, and H. Marvi, "Magnetic needle steering in soft phantom tissue," *Sci. Rep.*, vol. 10, no. 1, p. 2500, Feb. 2020.

[47] L. O. Mair et al., "MagnetoSuture: Tetherless manipulation of suture needles," *IEEE Trans. Med. Robot. Bionics*, vol. 2, no. 2, pp. 206–215, May 2020.

[48] K. Ishiyama, M. Sendoh, and K. I. Arai, "Magnetic micromachines for medical applications," *J. Magn. Mater.*, vol. 242, pp. 41–46, Apr. 2002.

[49] M. Sendoh, K. Ishiyama, K. I. Arai, M. Jojo, F. Sato, and H. Matsuki, "Fabrication of magnetic micromachine for local hyperthermia," *IEEE Trans. Magn.*, vol. 38, no. 5, pp. 3359–3361, Sep. 2002.

[50] A. W. Mahoney, N. D. Nelson, E. M. Parsons, and J. J. Abbott, "Non-ideal Behaviors of magnetically driven screws in soft tissue," in *Proc. IEEE Int. Conf. Intell. Robots Syst.*, 2012, pp. 3559–3564.

[51] N. D. Nelson, J. Delacenserie, and J. J. Abbott, "An empirical study of the role of magnetic, geometric, and tissue properties on the turning radius of magnetically driven screws," in *Proc. IEEE Int. Conf. Robot. Autom.*, 2013, pp. 5352–5357.

[52] B. Chaluvadi, K. M. Stewart, A. J. Sperry, H. C. Fu, and J. J. Abbott, "Kinematic model of a magnetic-microrobot swarm in a rotating magnetic dipole field," *IEEE Robot. Autom. Lett.*, vol. 5, no. 2, pp. 2419–2426, Apr. 2020.

[53] W. Lee, J. Nam, J. Kim, E. Jung, N. Kim, and G. Jang, "Steering, tunneling, and Stent delivery of a multifunctional magnetic catheter robot to treat occlusive vascular disease," *IEEE Trans. Ind. Electron.*, vol. 68, no. 1, pp. 391–400, Jan. 2021.

[54] C. M. Heunis, K. J. Behrendt, E. E. G. Hekman, C. Moers, J.-P. P. M. de Vries, and S. Misra, "Design and evaluation of a magnetic rotablation catheter for arterial stenosis," *IEEE/ASME Trans. Mechatronics*, vol. 27, no. 3, pp. 1761–1772, Jun. 2022.

[55] Z. Yang, L. Yang, M. Zhang, C. Zhang, S. C. H. Yu, and L. Zhang, "Ultrasound-guided catheterization using a driller-tipped guidewire with combined magnetic navigation and drilling motion," *IEEE/ASME Trans. Mechatronics*, vol. 27, no. 5, pp. 2829–2840, Oct. 2022.

[56] A. J. Petruska and J. J. Abbott, "Optimal permanent-magnet geometries for dipole field approximation," *IEEE Trans. Magn.*, vol. 49, no. 2, pp. 811–819, Feb. 2013.

[57] D. E. Usevitch, A. J. Sperry, and J. J. Abbott, "Translational and rotational arrow cues (TRAC) navigation method for manual alignment tasks," *ACM Trans. Appl. Percept.*, vol. 17, no. 1, pp. 1–19, Feb. 2020.

[58] D. C. Stewart, A. Rubiano, K. Dyson, and C. S. Simmons, "Mechanical characterization of human brain tumors from patients and comparison to potential surgical phantoms," *PLoS One*, vol. 12, no. 6, Jun. 2017, Art. no. e0177561.

[59] S. E. Wright, A. W. Mahoney, K. M. Popek, and J. J. Abbott, "The spherical-actuator-magnet manipulator: A permanent-magnet robotic end-effector," *IEEE Trans. Robot.*, vol. 33, no. 5, pp. 1013–1024, Oct. 2017.

[60] V. Pratt, "Direct least-squares fitting of algebraic surfaces," *ACM SIGGRAPH Comput. Graph.*, vol. 21, pp. 145–152, Jul. 1987.

[61] K. Cherry, *The Size of the Human Brain*, Verywell Mind, New York, NY, USA, May 2020.

[62] E. Buckingham, "On physically similar systems; illustrations of the use of dimensional equations," *Phys. Rev.*, vol. 4, no. 4, pp. 345–376, 1914.

[63] G. I. Barenblatt, *Scaling, Self-Similarity, and Intermediate Asymptotics*. Cambridge, U.K.: Cambridge Univ. Press, 1996.

[64] T. Watts, R. Secoli, and F. R. Y. Baena, "A mechanics-based model for 3-D steering of programmable bevel-tip needles," *IEEE Trans. Robot.*, vol. 35, no. 2, pp. 371–386, Apr. 2019.